

REPORT DOCUMENTATION PAGE

The public reporting burden for this collection of information is estimated to average 1 hour per response, including the time for reviewing instructions, searching existing data sources, gathering the data needed, and completing and reviewing the collection of information. Send comments regarding this burden estimate or any other aspect of this collection of information, including suggestions for reducing the burden, to the Department of Defense, Executive Service Directorate (0704-0188). Respondents should be aware that notwithstanding any other provision of law, no person shall be subject to any penalty for failing to comply with a collection of information if it does not display a currently valid OMB control number.

PLEASE DO NOT RETURN YOUR FORM TO THE ABOVE ORGANIZATION.

1. REPORT DATE (DD-MM-YYYY) 04-12-2010			2. REPORT TYPE Final Performance Report		3. DATES COVERED (From - To) 07/01/2006 to 12/14/2009	
4. TITLE AND SUBTITLE Computational Spectroscopy of Structured Carbon Nanotube Interfaces For Biochemical Sensing					5a. CONTRACT NUMBER	
					5b. GRANT NUMBER FA9550-06-1+ 0230	
					5c. PROGRAM ELEMENT NUMBER	
6. AUTHOR(S) David J. Brady Jeffrey T. Glass					5d. PROJECT NUMBER	
					5e. TASK NUMBER	
					5f. WORK UNIT NUMBER	
7. PERFORMING ORGANIZATION NAME(S) AND ADDRESS(ES) Duke University 334 North Building, Box 90077 Durham, NC 27708					8. PERFORMING ORGANIZATION REPORT NUMBER	
9. SPONSORING/MONITORING AGENCY NAME(S) AND ADDRESS(ES) AFOSR Dr. Kent Miller 875 N. Randolph Street Suite 324, Room 3112 Arlington VA 22203-1768					10. SPONSOR/MONITOR'S ACRONYM(S) AFOSR	
					11. SPONSOR/MONITOR'S REPORT NUMBER(S)	
12. DISTRIBUTION/AVAILABILITY STATEMENT Distribution A - Approved for public release						
13. SUPPLEMENTARY NOTES						
<div style="text-align: center; font-size: 2em; font-weight: bold;">20100602218</div>						
14. ABSTRACT Compressive measurement in spectroscopic and interferometric systems has been demonstrated. Computational spectroscopy studies resulted in the development of the coded aperture snapshot spectral imager (CASSI) and coherence measurement studies resulted in the development of compressive holography. We developed the theoretical underpinnings of coded aperture snapshot spectral imaging and designed two proof-of-concept systems: a pushbroom system (SmacM) and a snapshot system (MacSim). Iso-lated growth of nanoscale carbon nanotube (CNT) islands has been accomplished as well as growth via a Pt catalyst, including microstructural validation of the CNT structure using transmission electron microscopy. The use of Pt catalyst during the CNT growth rather than the more traditional CNT catalyst materials is beneficial due to the extensive study of SERS (Surface Enhanced Raman Spectroscopy) and new biological application areas are enabled due to Pt's approved use for in-vivo applications.						
15. SUBJECT TERMS spectroscopy, nanoscience, biochemical sensing						
16. SECURITY CLASSIFICATION OF:			17. LIMITATION OF ABSTRACT	18. NUMBER OF PAGES	19a. NAME OF RESPONSIBLE PERSON	
a. REPORT unclassified	b. ABSTRACT unclassified	c. THIS PAGE unclassified			David Brady	
					19b. TELEPHONE NUMBER (Include area code) 919-660-5394	

Final Performance Report

AFOSR Grant Number FA9550-06-1-0230

Descriptive Title: "Computational Spectroscopy of Structured Carbon Nanotube Interfaces for Biochemical Sensing"

Grantee Institution: Duke University, Electrical and Computer Engineering,
130 Hudson Hall, Durham, NC 27708-0291

Principal Investigator: David J. Brady

Co-Principal Investigators: Jeffrey T. Glass and Jungsang Kim

Reporting Period: July 1, 2006 to December 14, 2009

Table of Contents

Abstract.....	3
2. Objectives:	3
3. Status of effort:.....	3
4. Accomplishments/New Findings:	5
SmacM Multispectral Microscope	5
<i>Bichromatic Source</i>	6
<i>Broadband Source</i>	8
<i>Spatial and Spectral Reconstructions</i>	10
Target Classification	12
Carbon Nanotube Growth on Pt.....	16
<i>Scanning and Transmission Electron Microscopy of CNTs</i>	18
<i>Nanoscale Carbon Nanotube Island Growth</i>	20
Quantum Coherence Sensor.....	21
Compressive Holography.....	27
5. Personnel Supported:	30
6. Publications:	30
7. Interactions/Transitions:.....	31
a. Participation/presentations at meetings, conferences, seminars, etc.	31
b. Consultative and advisory functions	32
c. Technology Assists, Transitions, and Transfers.	32
8. New discoveries, inventions, or patent disclosures.	32
9. Honors/Awards:	32
References	32

Abstract

Compressive measurement in spectroscopic and interferometric systems has been demonstrated. Computational spectroscopy studies resulted in the development of the coded aperture snapshot spectral imager (CASSI) and coherence measurement studies resulted in the development of compressive holography. We developed the theoretical underpinnings of coded aperture snapshot spectral imaging and designed two proof-of-concept systems: a pushbroom system (SmaeM) and a snapshot system (MaeSim). Isolated growth of nanoscale carbon nanotube (CNT) islands has been accomplished as well as growth via a Pt catalyst, including microstructural validation of the CNT structure using transmission electron microscopy. The use of Pt catalyst during the CNT growth rather than the more traditional CNT catalyst materials is beneficial due to the extensive study of SERS (Surface Enhanced Raman Spectroscopy) and new biological application areas are enabled due to Pt's approved use for in-vivo applications.

2. Objectives:

The initial goals of this program were

1. To design and demonstrate a platform for hyperspectral Raman microscopy based on results from previous AFOSR supported work in computational sensor design.
2. To use the computational hyperspectral microscope to explore spatial and spectral signatures of Raman signals generated on patterned substrates of carbon nanotubes.
3. To functionally outline optical signals and nanotube-analyte interactions capable of enabling advanced chemical sensors and
4. To detail charge transport and molecular interactions in CNT devices for sensing and photonic devices.

Supplemental funding was added to the program in 2009 through the DARPA MTO effort "quantum coherence sensing." The objective of the extended program was to explore the possibility of direct measurement of optical coherence functions using quantum interferometry. Study of coherence sensors resulted in the discovery of compressive holography.

3. Status of effort:

This program resulted in major advances in the use of compressive sampling theory to reconstruct 3D data volumes from snapshot 2D measurements. According to previous theory, 3D reconstruction required temporal scanning. Under this program we demonstrated 3D spectral data cube reconstruction from a single coded 2D measurement. Under the extended effort focusing on coherence sensing, we further demonstrated 3D tomographic image reconstruction from a single 2D Gabor hologram. These developments hold substantial promise for applications in hyperspectral remote sensing and laser radar.

A Hadamard Aperture Microscopic Multiple Excitation Raman spectrometer has been designed, constructed, and its operation verified. We developed the theoretical underpinnings of the aperture coded spectral engine and designed two proof-of-concept systems: a pushbroom system (SmaeM) and a snapshot system (MacSim). The pushbroom system is based on a static aperture coded single disperser design that is translated in order to capture a 3D cube (2D spatial, 1D spectral). The snapshot system, however, is a dual disperser architecture which uses advanced signal processing techniques (*compressive sensing*) to measure a 3D cube in a snapshot. The basic snapshot design is called a Coded Aperture Snapshot Spectral Imager (CASSI). Imagers based on this design computational sensors that are able to recover a 3D datacube representing spatial and spectral information at every pixel in an image of a scene using just one snapshot 2D projection. CASSI instruments utilize a coded aperture and one or more dispersive elements to modulate the optical field from a scene. A detector captures a two-dimensional, multiplexed projection of the three-dimensional datacube representing the scene. The nature of the multiplexing performed depends on the relative position of the coded aperture and the dispersive element(s) within the instruments. Experimental results from our proof-of-concept implementation of a hyperspectral microscope have been obtained for applications in addition to simple Raman spectrometers.

Isolated growth of nanoscale CNT islands has been accomplished as well as growth via a Pt catalyst, including microstructural validation of the CNT structure using transmission electron microscopy. Plasma enhanced chemical vapor deposition has been utilized to grow vertically aligned multiwall carbon nanotubes (CNTs) via a platinum catalyst. A thermally oxidized layer of SiO_2 served as a diffusion barrier to prevent Pt silicide formation and was shown to aide the formation of well dispersed catalytic nanoparticles. Adjustment of the catalyst film thickness was effective for varying the diameter and density of synthesized CNTs. TEM analysis revealed a bamboo-like structure with catalyst particles in the tips, root, and within internal compartments, indicating that the catalyst was in a liquid state during growth. The use of Pt catalyst during the CNT growth rather than the more traditional CNT catalyst materials is beneficial due to the extensive study of SERS (Surface Enhanced Raman Spectroscopy) utilizing Pt. In addition, new biological application areas are enabled by using Pt due to its approved use for in-vivo applications.

This program was extended for 1 year under DARPA MTO seedling support focusing on coherence measurement and compressive sampling. One goal of this portion of the study was to analyze the feasibility and physical implementation of quantum coherent optical sensors. As part of the seedling effort, we performed a careful theoretical study on utilizing quantum coherence to perform optical coherence measurement, and identified a physical system and device concept to realize coherence measurement using quantum interactions. The debate on the potential advantage of utilizing quantum systems for direct measurement of optical coherence between two fields with better SNR than the classical limit has not quite been conclusively settled. Based on the technologies available today, physical realization of such coherence measurement remains a major challenge. The second goal of this portion of the study was to explore the use of classical detectors to measure compressive projections of coherence functions. This portion of the study was extremely successful, as demonstrated in the development of compressive ho-

lography. We demonstrated independent 3D tomographic data cube of various samples using compressive holography.

4. Accomplishments/New Findings:

SmacM Multispectral Microscope

A second generation scanning (pushbroom) multispectral aperture coded microscope (SmacM) applied to fluorescence studies has been constructed[1].

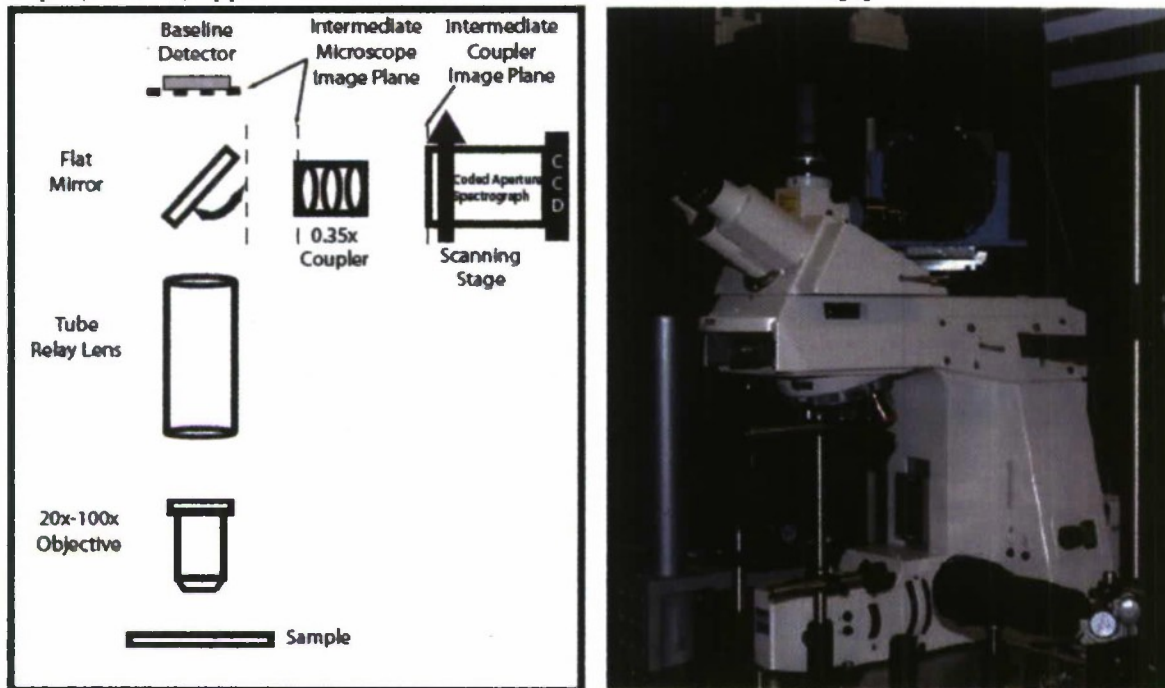


Figure 1: (Left) Second-generation system schematic. (Right) Second-generation system photograph.

An aperture- coded spectrometer is interfaced with one of the exit ports on the *Zeiss Axioplan 2* microscope and translated perpendicular to the dispersion direction of the spectrometer. Coupling optics spatially de-magnify the field size at the exit port of the microscope such that it more accurately maps to the maximum field size accepted by the aperture coded spectrometer. Translation of the spectrometer is completed using a three-axis stage controller that interfaces with a *Newport ESP 300* motion controller. The z-focusing capability for the microscope is automated using another three-axis motion controller. The *Zeiss Axioplan 2* microscope was modified (sample chamber and condensing optics were completely removed) for laser excitation fluorescence studies.

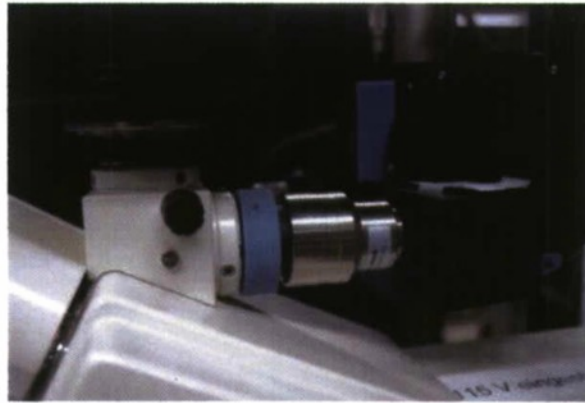


Figure 2: At the intermediate image plane of the microscope where the image is de-magnified with a CCTV 0.35x *Nikon* coupler and interfaced with an aperture-coded spectrometer.

Two focal planes are used in the setup for SmacM. One CCD is located at the back-end of the aperture coded spectrometer and the baseline camera is located at the second output port of the microscope. The baseline camera is a SPOT CCD made by *Diagnostic Instruments* is a multispectral camera that measures three spectral channels from an image using a liquid crystal tunable filter. Both of the CCDs can be seen in Figure 2.

Bichromatic Source

As a proof-of-concept test, a quartz on chrome 64 x 64 grid, 5.4 μm mask with the letters "DISP" is illuminated with a 10x beam expanded Helium Neon and green Helium Neon laser profile. Each slice in the data cube takes less than a second to collect. A total of 223 steps are collected over a 12mm extent. Figure 3 represents slices from the data cube collected from a spectrally bichromatic source.

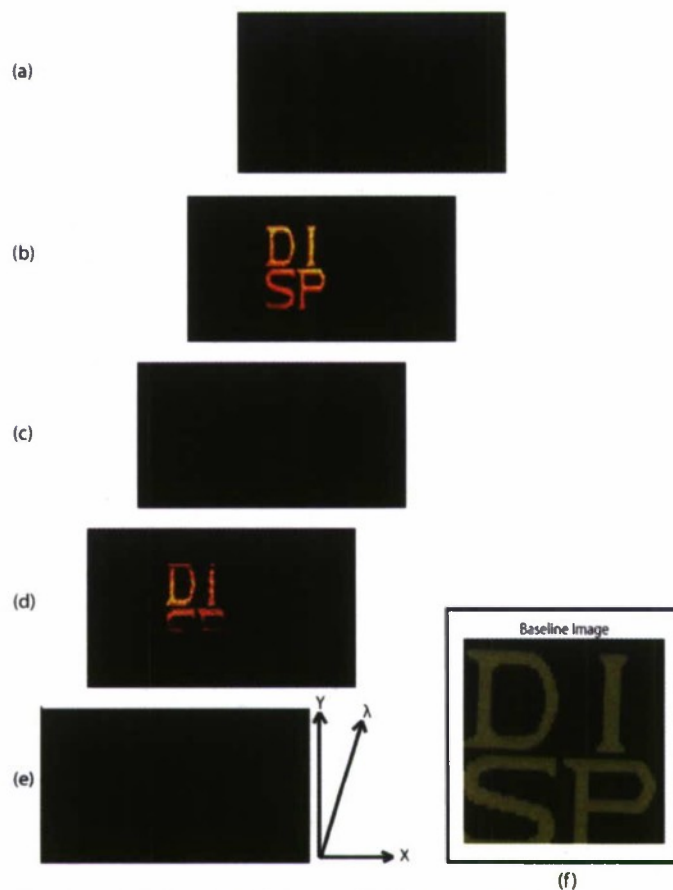


Figure 3: Datacube generation for a two-lined source illumination of a chrome on quartz mask (DISP). (a) Image at spectral channel $N = 15$. (b) Image at spectral channel $N = 97$ showing a mask pattern obtained from the HeNe. (c) Image at spectral channel $N = 150$. (d) Image at spectral channel $N = 248$ showing the full mask pattern from the green HeNe (e) Image at spectral channel $N = 350$ (f) Baseline 2D spatial image obtained with the SPOT camera with a different field of view.

A plot of a row of voxels at a particular spatial location through the data cube shows two delta like peaks at the wavelengths corresponding to the helium neon (632.8nm) and green helium neon peaks (543.5nm). Spectral slices appear in the green at high spectral channels and red at lower spectral channels for the reconstructed data cube.

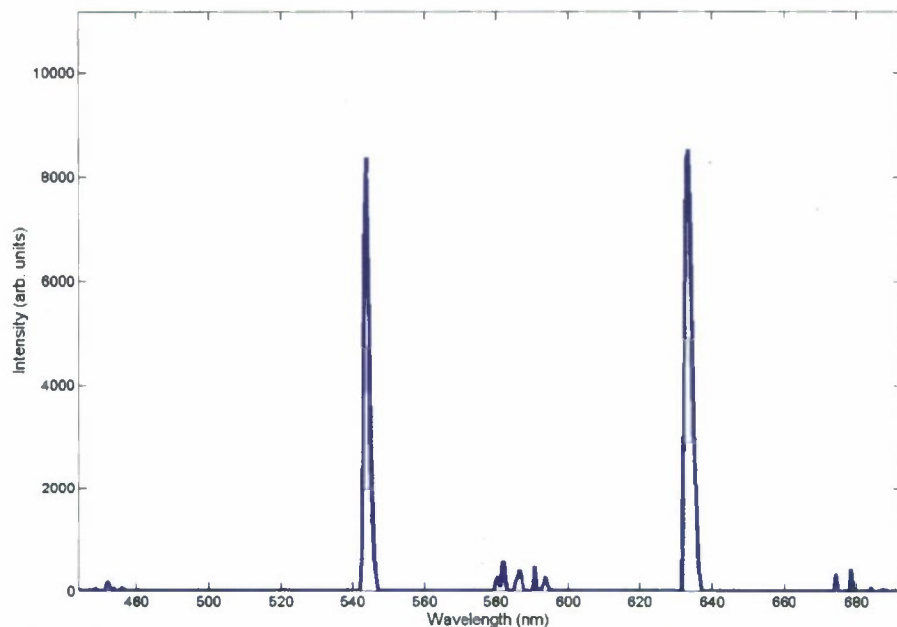


Figure 4: Plot for a row of voxels in a data cube. Peaks from the green HeNe laser source and HeNe laser source are shown.

Broadband Source

Broadband sources were also tested with SmaeM. Three types of fluorescent microspheres (Fluospheres) from *Invitrogen* were tested. The fluorescent microspheres were prepared in a 10:1 solution with de-ionized water. A droplet from a poly-l-lysine solution is placed on the microscope slide before adding the fluospheres to increase the adhesion process of the fluospheres to the microscope slide. De-ionized water is then used to wash the droplet off of the microscope slide for image acquisition with the instrument. The fluospheres tested consisted of 0.04 μ m red-orange fluorescent (565/580) carboxylate-modified microspheres, 0.2 μ m orange fluorescent (540/560) carboxylate-modified microspheres, and 1.0 μ m Nile red fluorescent (535/575) carboxylate-modified microspheres. Spectra for the fluorescent microspheres were first collected with a conventional slit spectrometer, Ocean Optics, as a baseline test. Results with the aperture coded spectrometer were then compared with the baseline results.

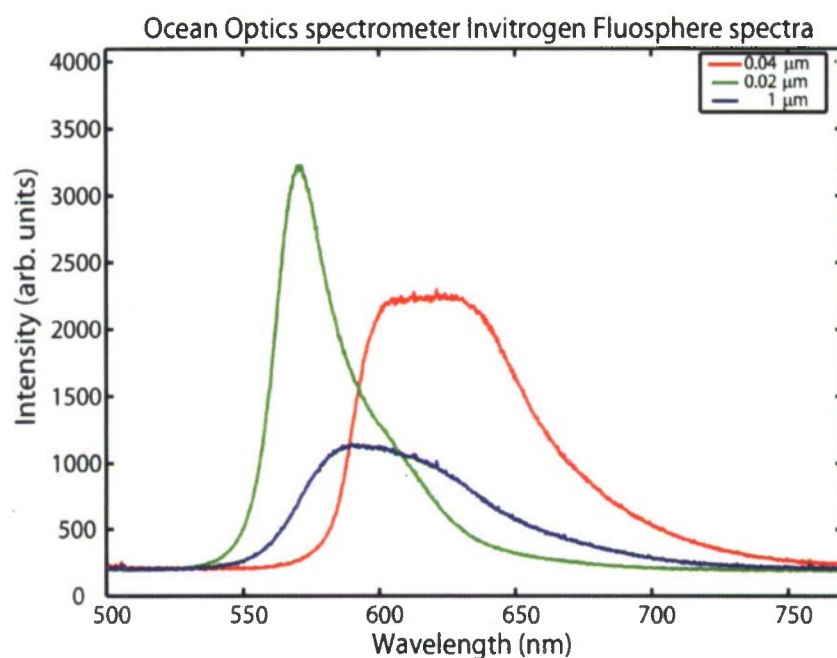


Figure 5: Overlay of fluorescent microsphere emission spectra.

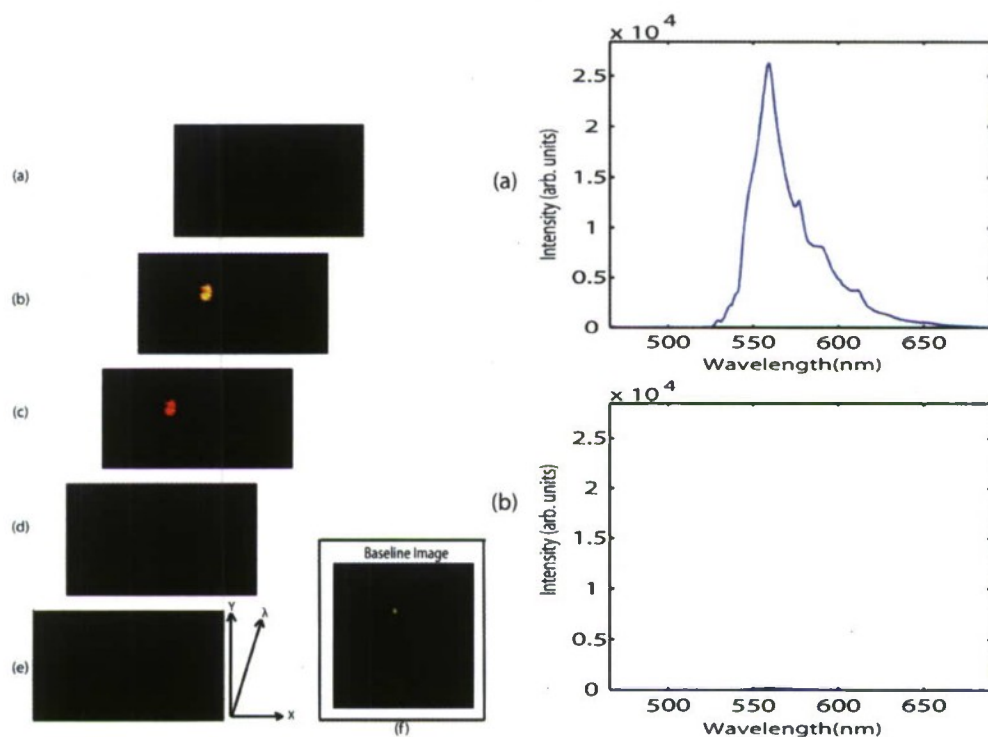


Figure 6: Data cube generation for 0.2 μm fluorescent microspheres excited by 532 nm laser light. (a) Spectral channel $N = 268$. (b) Spectral channel $N = 222$. (c) Spectral channel $N = 205$. (d) Spectral channel $N = 128$. (e) Spectral channel $N = 10$. (f) Baseline image (right) (a) Plot along the spectral channels of the data cube for an "on" pixel. (b) Plot along the spectral axis of an "off" pixel.

Figure 6 shows the results obtained from the 0.2 μ m fluorescent microsphere test. A baseline image is used to compare the spatial resolution of the reconstructed spectral slices for a given data set. When plotting a row of voxels at a spatial location defined by the fluorescent sphere, a fluorescence spectral profile is obtained. This spectral profile can be compared to that obtained from a slit spectrometer as seen in Figure 5.

Spatial and Spectral Reconstructions

Testing spatial and spectral reconstructions from fluorescent microspheres is a baseline test conducted with confocal imaging systems. The next step in verifying the applicability of the SmaeM system to fluorescence microscopy studies is to analyze fixed-cellular assays. Data with SmaeM was taken from a FluoCell microscope slide #2 from *Invitrogen*. The slide contained bovine pulmonary artery endothelial cells stained with red-fluorescent Texas Red-X phalloidin for labeling F-actin, mouse monoclonal anti-alpha-tubulin, green-fluorescent BODIPY FL goat anti-mouse IgG was used to label microtubules and blue-fluorescent DAPI was used to label the nuclei. Due to the sensitivity of SmaeM only two (red & green) out of the three fluorescent signals could be detected. The slide was again excited with 532nm light and imaged through a 50x objective, NA = 0.5 and a 0.35x coupling optic.

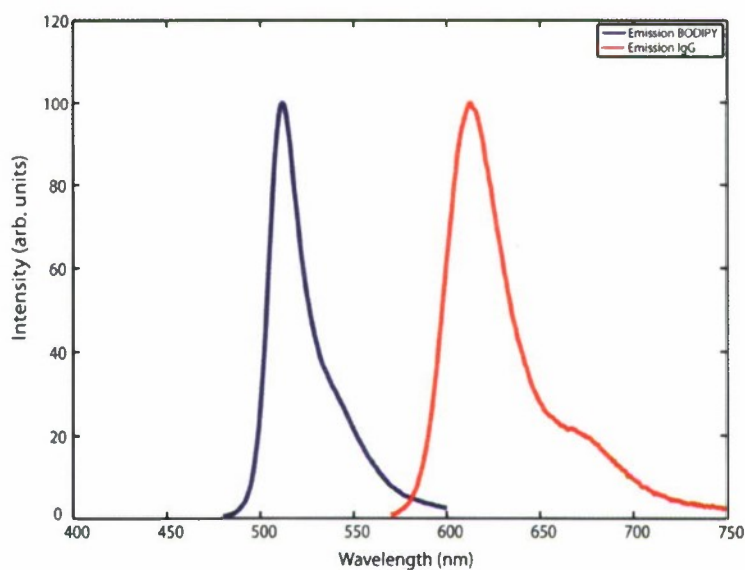


Figure 7: *Invitrogen* cell slide: Emission spectra from BODIPY and IgG fluorescent labels in the bovine pulmonary artery endothelial cell.

Figure 7 describes the baseline emission profiles from two of the fluorescence signals from the *Invitrogen* slide.

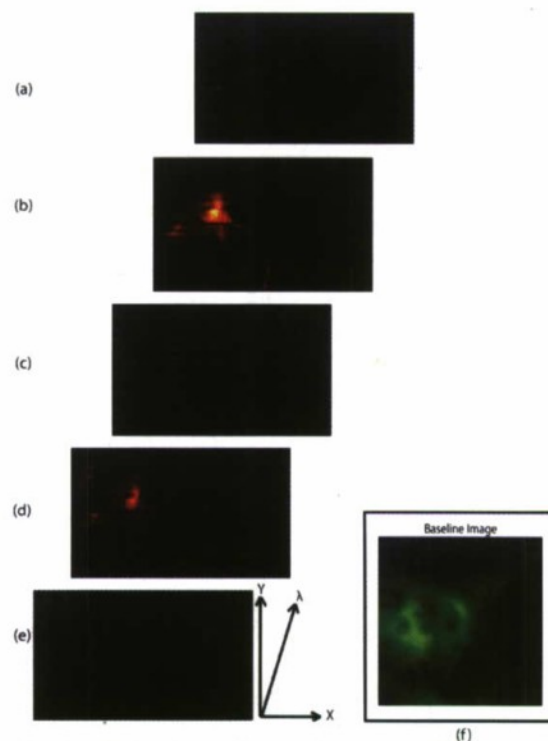


Figure 8: Data cube generation for the bovine cell on a microscope slide excited by a 532nm laser source. (a) Spectral channel $N = 310$ (b) Spectral channel $N = 275$. (c) Spectral channel $N = 228$. (d) Spectral channel $N = 121$. (e) Spectral channel $N = 10$. (f) Baseline image for the bovine endothelial cell with the SPOT camera.

Figure 8 describes the reconstructed data cube obtained for the bovine endothelial cell. Compared to the baseline image the spatial resolution of the reconstructed slices could be improved. The two fluorescent signals are distinguished within the data cube.

Target Classification

Under a previous AFOSR grant #3136057, we have developed a spectrally adaptive signal segmentation algorithm that allows the direct classification of targets[2]. To demonstrate the classification capabilities of the algorithm we have used as a test bed a DD-CASSI imager incorporated into a Zeiss AxioObserver A1 fluorescence, microscope (MacSim), see Figure 9

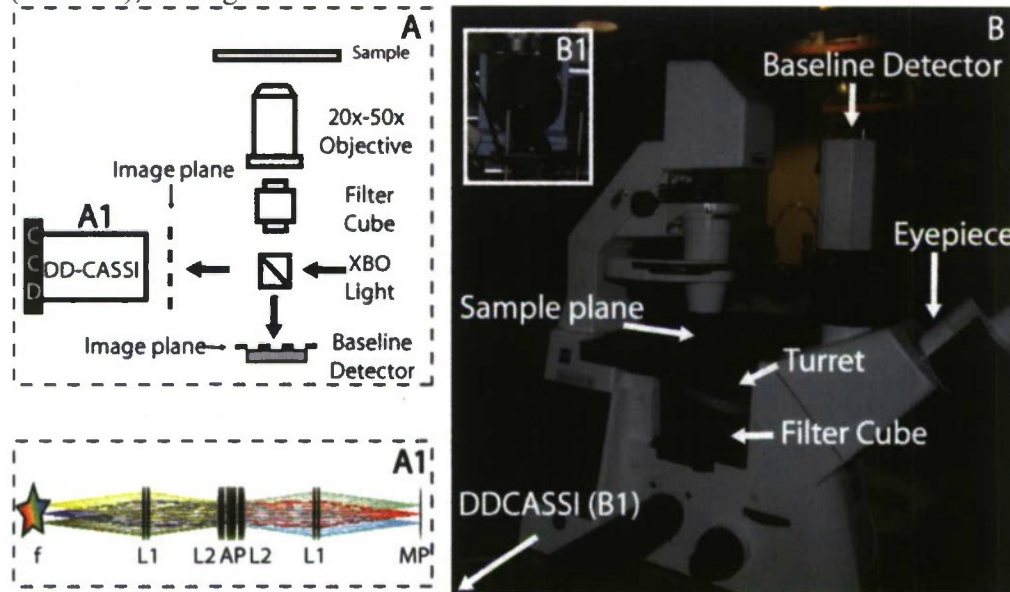


Figure 9: (A) System layout with a Zeiss AxioObserver A1 upright microscope. (A1) Zemax layout for the Arm 1 in the DD-CASSI optical design.(B) Experimental setup. (B1) DD-CASSI interfaced with the output port of an upright microscope.

In collecting the data a spectrum is reconstructed at every pixel location in the image using a total variation (TV) minimization compressive sensing algorithm. The object being imaged contains polystyrene microspheres with ten unique spectral emissions shown in

Figure 10. A total variation (TV) minimization algorithm is then adapted for image segmentation of the recorded spectral image. To segment the image, *a priori* knowledge of the spectral signatures expected in the image or used during the segmentation process. The instrument in Figure 9 records 31 spectral channels spanning the spectral range between 450nm and 730nm with 10nm resolution.

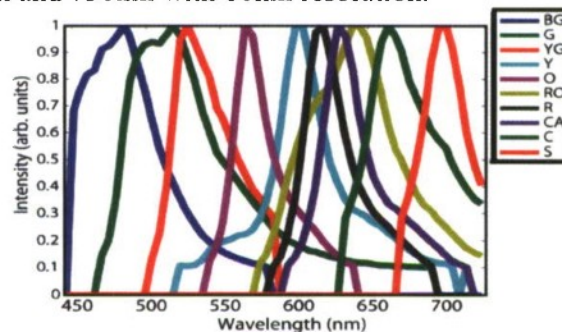


Figure 10: Spectral profiles for different fluorescent microspheres.

A two-step iterative, shrinkage and thresholding algorithm (TwIST) has been adapted to estimate the 3D (x,y,λ) data cube from a 2D snapshot taken by the CASSI system. To identify the desired signatures a spectrally adaptive image segmentation algorithm based a total variation minimization compressive sensing algorithm was applied. The result is a 3D data cube, $f(x,y,\lambda)$, estimate projected into a lower dimensional texture-based data cube, $\theta(x,y,n)$. Each texture is associated with a spectral signature, \mathbf{n} , unique to the sample. The new spectrally textured data cube records the type (\mathbf{n}) of each pixel registered, as well as, the brightness value associated with pixel location. In Figure 11, a transformation from \mathbf{f} to θ is described. Each \mathbf{n} value corresponds to an associated spectral signature for the cube layer.

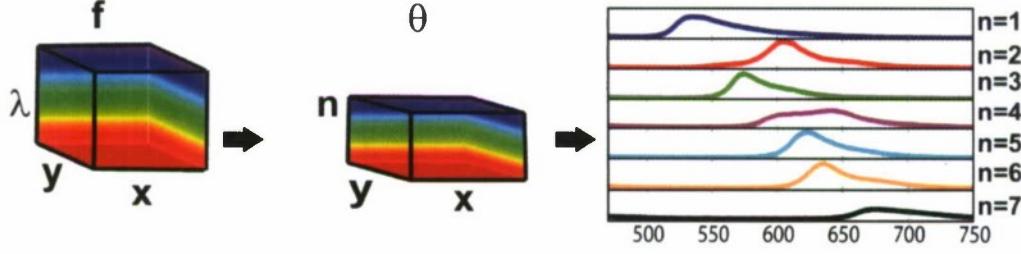


Figure 11: Transformation of the $f(x,y,\lambda)$ data cube into a lower dimensional $\theta(x,y,n)$ datacube

The transformation of \mathbf{f} to θ is represented by

$$\mathbf{f} = \mathbf{W}\theta$$

$$\theta^* = \arg \min_{\theta} \|\mathbf{g} - \mathbf{H}\mathbf{W}\theta\|_2^2 + \tau \Phi_{TV}(\theta)$$

$$\Phi_{TV}(\theta) = \sum_{i,j} \sqrt{(\theta_{i+1,j} - \theta_{i,j})^2 + (\theta_{i,j+1} - \theta_{i,j})^2} = \sum_{i,j} |(\nabla \theta)_{i,j}|$$

Again a total variation minimization approach is used to converge to an image with the sparsest gradient. In the above equations, \mathbf{H} is a positive, semi-definite matrix, \mathbf{g} is the intensity recorded at the focal plane, θ is an estimate, τ is the regularizing parameter that minimizes the ill-posed nature of the problem, and ϕ is the regularizing function that applies a gradient along the rows and columns of the cube estimate. Figure 12 provides an intuitive example of how a gradient impacts an image. Four squares are used to model fluorescent microspheres of different spectral emission and different intensities. A gradient is similar to an edge detection filter as seen in the diagram below.

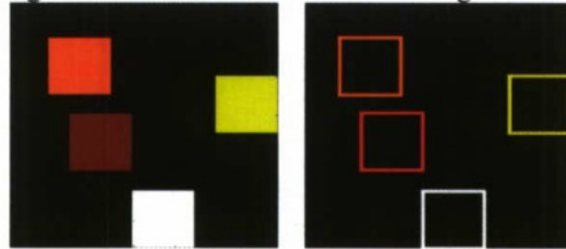


Figure 12: Demonstration of the use of total variation minimization to produce the sparsest gradient of an image. Here four squares of unique color are reduced to outlines of the squares.

An algorithm flow diagram is shown in Figure 13. An image is recorded by CASSI instrument in Figure 9 and intensity normalized. The 1200×1600 image is cropped to a local region corresponding to the field of view of single bead, \mathbf{g} . For the adaptation of TwIST for image segmentation, prior information in the form of a norma-

lized spectral database, W , and a cube, C , corresponding to a spectral impulse response every 5nm between 450nm-730nm is provided to the algorithm.

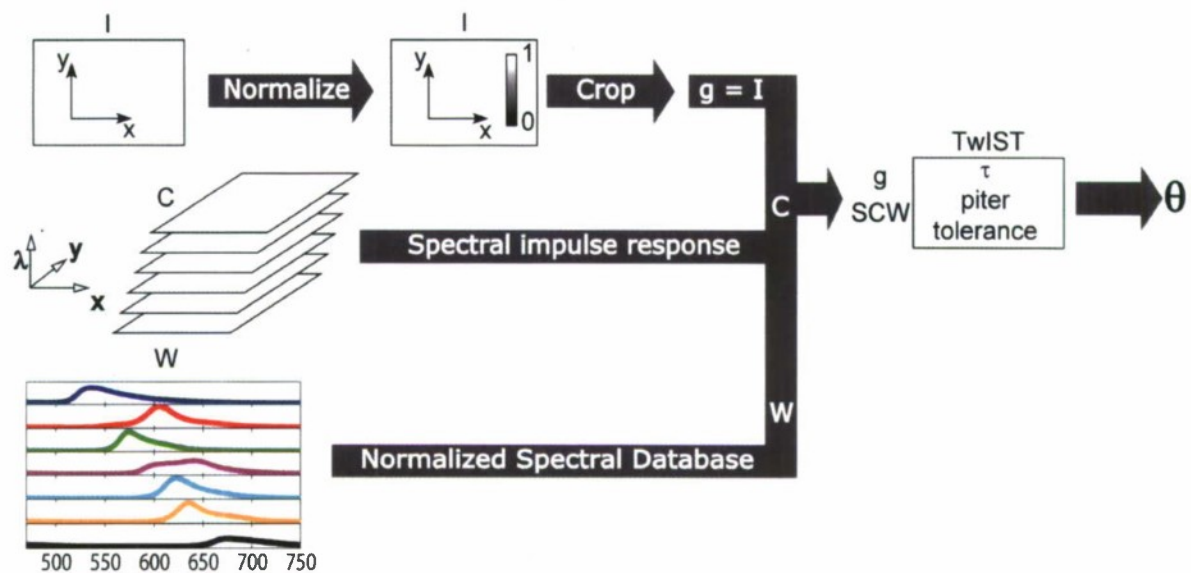


Figure 13: Image segmentation algorithm flow diagram

Filtered light from a Xenon arc lamp attached to the microscope with a bandwidth from 377nm to 396nm is used to excite the polystyrene microspheres that make up the samples. An intermediate image plane is formed at the output ports of the microscope. The DD-CASSI is interfaced to the microscope via the output port and captures the emission bandwidth from 420nm-800nm. A baseline, RGB detector is placed at the second output port of the microscope. A high frame rate camera that allows dynamic scene analysis and a cooled, long exposure capable camera for static samples can be used to record the output of the CASSI.

A fluorescent scene recorded by the CASSI system is shown in Figure 914. The image contains all ten bead varieties.

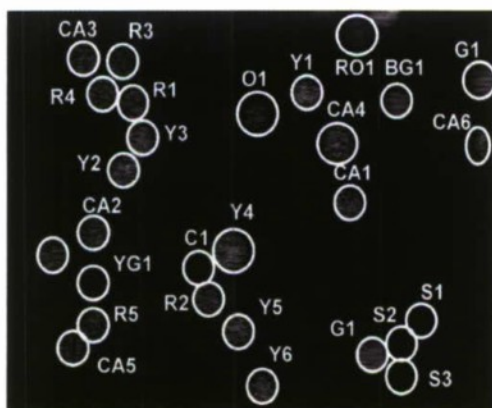


Figure 14: Raw DD-CASSI image

An RGB baseline image is obtained from the second port

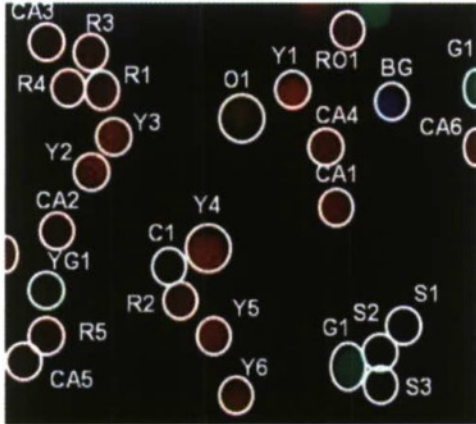


Figure 15: RGB image of a fluorescence scene.

It is a challenge to distinguish between the ten different bead varieties shown in Figure 154. Using the image segmentation algorithm we have developed, a bead identity map (or spectral texture-based map) clearly allows one to distinguish all ten bead varieties, as shown in Figure 16.

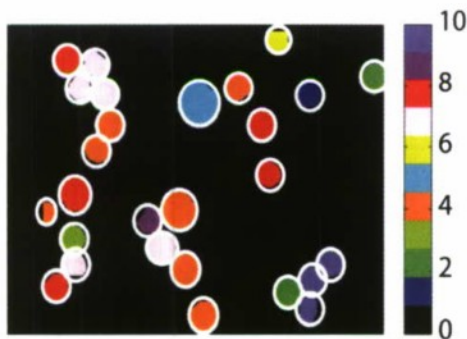


Figure 16: Image segmentation results

Figure 17, displays a pseudo-color estimate from reconstructed data.

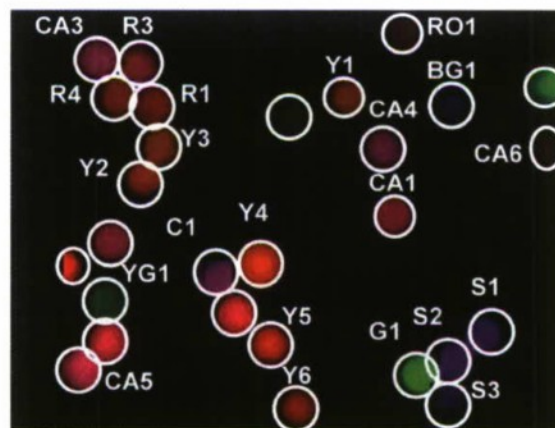


Figure 17: Pseudo-color image of fluorescent beads.

In summary, coded aperture snapshot spectral imager has been constructed and applied to fluorescence microscopy applications. A total variation minimization algorithm has been applied to the CASSI snapshot spectral imager to allow a spectrum to be reconstructed at every pixel location in an image. The algorithm developed allows the use of image segmentation based on texture to be used for fluorescence bead analysis. Both static and dynamic fluorescent beads have been analyzed.

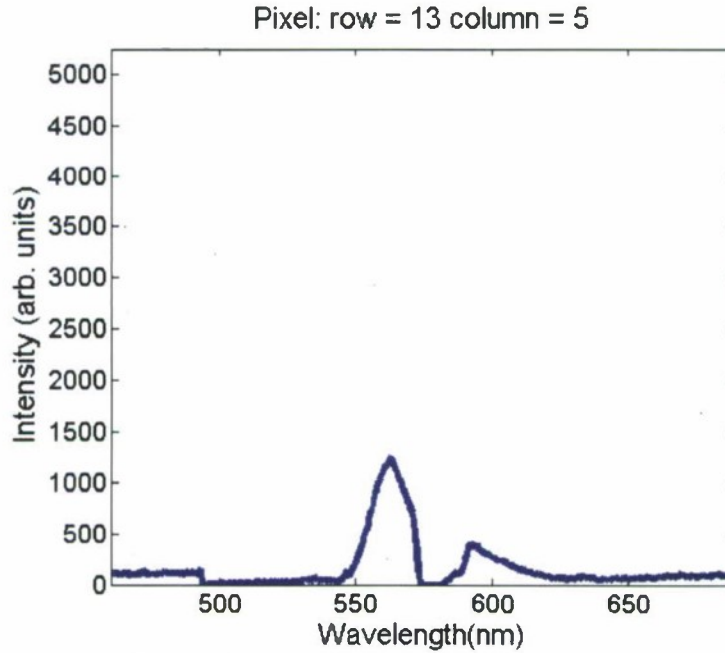


Figure 18: Plot along the spectral channels for a given pixel location.

Carbon Nanotube Growth on Pt

Sample preparation involved cleaving silicon (100) wafers to desired size and ultrasonically cleaning in solvent. The substrates were then dried in nitrogen and oxidized in a tube furnace at 1000°C in dry O₂ for 2 hours and allowed to cool overnight. The resulting oxide thickness was ~ 200 nm. Pt thin films of three different thicknesses (15, 34, and 50 Å) were deposited on the oxidized substrates using a CHA Electron-beam Evaporation system. Pt-coated substrates were then placed in a 915 MHz M-PECVD reactor and pumped down to < 10 mTorr in preparation for CNT growth. The use of ammonia or hydrogen plasma for pretreatment resulted in similar CNT growth morphology with the exception that ammonia pretreatment yielded slightly better vertical alignment. The presence of nitrogen species is known to enhance nucleation during MPECVD growth creating a higher density of CNTs which have a greater interaction via van der Waals forces promoting growth along the same direction. This effect would be enhanced as CNTs grow longer. Nevertheless, for the remainder of this report we will simply refer to hydrogen or ammonia similarly as reducing gas or plasma.

Prior to growth, the substrates were heated to 1000°C in 100-150 sccm of reducing gas, followed by striking and stabilizing a reducing plasma at 21 Torr and 21 kW of magnetron input power. It should be noted that the growth temperature specified is the temperature setting of the substrate heater and does not accurately reflect the temperature of the sample due to its distance from the thermocouple measurement device and also heating induced by the plasma itself. Substrates were then pretreated for 1 minute under the stabilized reducing plasma. The total heat-up and pretreatment time was not more than 5 minutes during which the Pt film dewetted into discrete nano-sized islands. Following pretreatment, the reducing gas flow was halted and a mixture of methane and ammonia gas with a gas ratio of 3 - 5 CH₄/NH₃ was introduced into the plasma to initiate the growth of CNTs. Total flow rates did not exceed 200 sccm and growth times did not exceed 6 minutes.

The monitoring of nanoparticle evolution was critical for the successful growth of Pt-CNTs as the conditional process space was found to be much narrower than that for Fe-CNT growth with similar substrate material in our reactor. For instance, Pt-CNT growth did not occur at < 1000°C no matter the change in various other experimental parameters including growth gas ratio, pretreatment or growth time, catalyst thickness, etc. Figure 19 presents cross-section SEM micrographs of nanoparticle evolution following different pre-growth conditions.

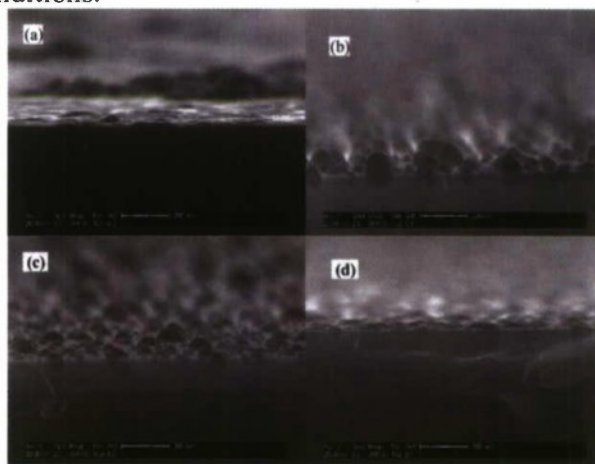


Figure 19: Cross-section SEM images showing nanoparticle evolution after reducing plasma pretreatments at 1000°C for, (a) 50 Å Pt / Si after 1 minute, and (b) 50 Å Pt / 2000 Å SiO₂ / Si after 1, (c) 3, and (d) 10 minutes.

It was observed that without the SiO₂ layer, a 3-dimensional network of discrete and spherical Pt nano-islands did not form. When the oxidized layer was present, discrete hemispherical shaped Pt nano-islands could be obtained under the reducing plasma although an increase in pretreatment time resulted in flatter and more round nano-islands. Interestingly, the Pt nano-islands were also partially embedded in the SiO₂ layer and the depth of partial submergence increased with pretreatment time. This change in catalyst island morphology with increasing pretreatment time is believed to have resulted in increased carbon encapsulation of Pt nano-islands yielding very short CNT lengths (< 200 nm) and eventually no CNT growth at all during the growth stage. However, it is believed that the porous silica layer may help isolate and prevent agglomeration of the Pt nano-islands as well enhance catalytic efficiency of Pt particles and thereby promote the growth of CNTs.

X-ray diffraction (XRD) has previously been effectively utilized to identify ultra-thin platinum silicide films deposited on (100) silicon and was thus used to investigate the possibility of substrate-catalyst interactions in this study. Phase analysis experiments were conducted via a Philips X'Pert PRO MRD HR XRD System to monitor the atomic bonding configurations at the interface of the deposited Pt film on the substrate materials before and after pretreatments. The X-ray source delivered primarily Cu K α X-rays with an incident wavelength of 1.5405 Å. Weaker diffraction peaks from Cu K β radiation were also observed in the resulting spectra when the Cu K α diffraction signal was intense, which occurred when probing the Si wafer. As-deposited Pt/Si substrate exhibited a broad peak at 39.8° which corresponds to a disordered Pt (111) lattice structure. Interestingly, after a pretreatment time of one minute, the Pt (111) peak is significantly diminished in the XRD spectrum and becomes absent after 10 minutes. Simultaneously, many small peaks attributed to various crystallographic orientations of platinum silicide (JCPDF #710523) arise.

Alternatively, XRD confirmed that the SiO₂ interlayer acted as a diffusion barrier to silicide formation during the pretreatment conditions. A sharp Pt (111) peak was detected after a 1 min pretreatment in reducing plasma indicating that the dewetted Pt metal was able to crystallize and form the hemispherical nanoparticles shown in Figure 19. However, as the pretreatment time was extended, the amount of crystalline Pt was continually reduced, and after 10 minutes, the amount of Pt (111) phase was below the instrument's detection limit. No other peaks besides those attributed to Pt (111) and the Si substrate were detectable within the acquired range contrary to what was observed after pretreatment when the SiO₂ interlayer was absent. The loss of crystalline Pt at longer pretreatment times may be due to sublimation, or diffusion of Pt atoms within the SiO₂ interlayer creating a diffuse impurity within the SiO₂ lattice. The submergence behavior previously discussed and depicted in Figure 19 favors the latter hypothesis. Ultimately, the XRD results of pretreated CNT substrates reflect observations noted in the SEM images and further study of substrate-catalyst interactions may have implications for promoting the efficiency of Pt-CNT growth.

Scanning and Transmission Electron Microscopy of CNTs

High-resolution cross-section and plan-view SEM images of successful Pt-CNT growth using short duration (≤ 1 min.) pretreatments for three different catalyst thicknesses are shown in Figure 20.

Catalyst thickness was an effective parameter for controlling density and CNT diameter. Given the relatively high surface tension of Pt compared to silicon dioxide, the formation of nano-islands on SiO₂ is expected to adhere to the Volmer-Weber growth mode. Therefore as a result of pretreatments, thinner catalyst films resulted in a higher density of smaller nano-islands and thus forming a dense forest of Pt-CNTs with smaller diameters (a, b). Likewise, thicker catalyst films resulted in a lower density of larger nano-islands which formed by ripening and coalescence. These formed larger diameter Pt-CNTs and a lower density film (e, f). A Pt film thickness of ~ 8 nm did not produce successful growth of CNTs as resulting nanoparticles were too large to support CNT growth. The average diameter of CNTs synthesized from 15, 34, and 50 Å thick Pt catalyst films were 14, 28, 60 nm respectively. In all cases, Pt-CNTs had uniform diameter distributions which did not exceed a range of ~ 30 nm.

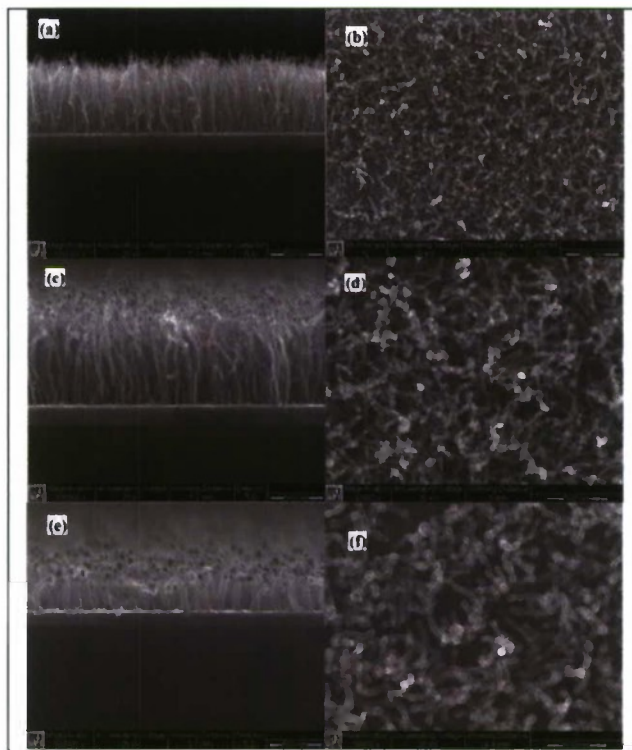


Figure 20: Cross-section (left column) and plan-view (right column) SEM images of Pt-CNT growth given the following Pt film thicknesses, (a) and (b), 15 Å; (c) and (d), 34 Å; and (e) and (f), 50 Å.

SEM images also clearly show catalyst particles in the tips suggesting a tip growth mode, although particles were also seen at the root and within the Pt-CNTs (which is discussed further in the TEM analysis section). The tip-growth mode has recently been shown to correlate with greatly reduced growth rates. This is associated with significant reshaping of catalyst nanoparticles and premature carbon encapsulation during CNT formation due to a weak support-catalyst interaction and fast self-diffusivity of the catalyst metal. Encapsulated Pt particles in our CNTs were typically elongated and greatly reshaped. Recently, a transition from tip-growth mode to a base-growth mode for randomly oriented Pt-CNTs has been reported in which the carbon yield was significantly improved. Experimental parameters of our PECVD system were controllably varied in a design of experiments in an attempt to extend the length or thickness of the Pt-CNT films, however this effort was unsuccessful. Goals of future work include modification of substrate materials to increase catalytic efficiency and longevity to sustain growth of longer aligned Pt-CNTs.

Low resolution TEM was utilized to inspect the internal structure of the Pt-CNTs. Preparation of TEM samples consisted of sonicating as-deposited samples in a 1:1 mixture of 20 mL of acetone and ethanol for 20 minutes to remove Pt-CNTs from the sub-

strate and reduce agglomeration. Then using a pipette, drops of the resulting solution were placed on a carbon holey film supported by a copper mesh TEM grid. The image in Figure 21 clearly shows a bamboo-like structure given the series of hollow and periodically stacked cone-shaped compartments. Again, catalyst particles are easily seen at the tips of the CNTs suggesting a tip-growth mode. However, upon further inspection, catalyst particles are also commonly seen at the root of the CNTs and the thickness of the inner walls decrease from tip to root along the hollow compartments.

The orientation of the cone-shaped catalyst particle encapsulated at the tip of the CNT is opposite the orientation of most of the cone-shaped compartments along the length of the CNT which have the same orientation as the catalyst particle at the root. In addition, some catalyst is occasionally observed within compartments along the length of the tube. Furthermore, the catalyst particles encapsulated at the tips are significantly larger than the diameter of the corresponding nanotube. This suggests that during high temperature growth the catalyst metal is in a liquid state and increasingly more parts of the particle will be sucked into and toward the growth front of nanotube due to capillary forces. Overall, these observations for the present Pt-CNT growth, suggest that the catalyst particles anchored at the root by the oxidized silicon substrate determines the growth of the nanotube via a base-growth mode, and the catalyst particle at the tip is actually not active. In fact, the depletion of the initial platinum particle at the root being sucked toward the tip may contribute to the cessation of Pt-CNT growth. However, more characterization is needed to confirm the details of the growth mechanism.

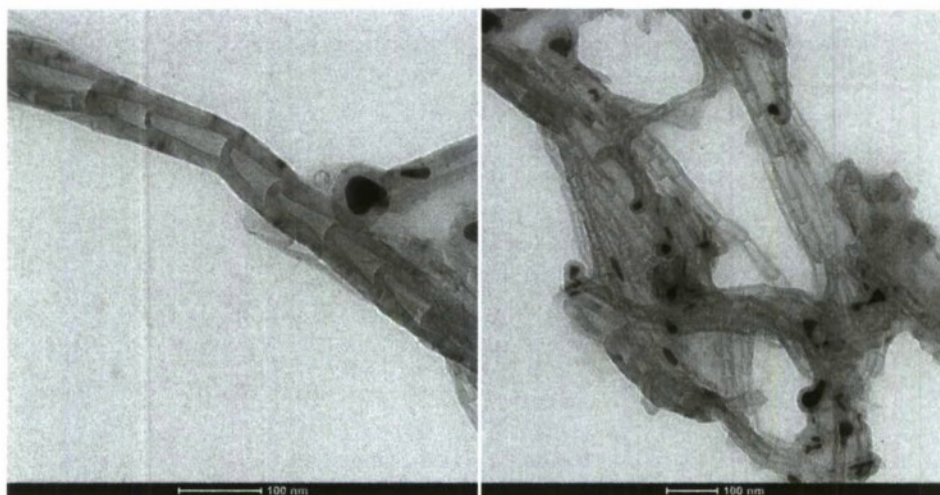


Figure 21: TEM images exhibiting bamboo-like structure consisting of hollow, truncated conical compartments and tip of Pt-CNT with encapsulated Pt particle

Nanoscale Carbon Nanotube Island Growth

Using a FIB (Focused Ion Beam) to define the Pt catalyst area, nanoscale CNT Islands can be grown (Acknowledgement: Anuj Dhawan). The sample shown in Figure 22 was grown with 50 angstrom of platinum and a 150:50 Methane:Ammonia ratio at 900C. These islands will enable controlled sensing measurements with well defined CNT volumes. Future work will utilize Raman spectroscopy to examine these Pt catalyzed CNTs

with varying nano-island dimensions and analytes.

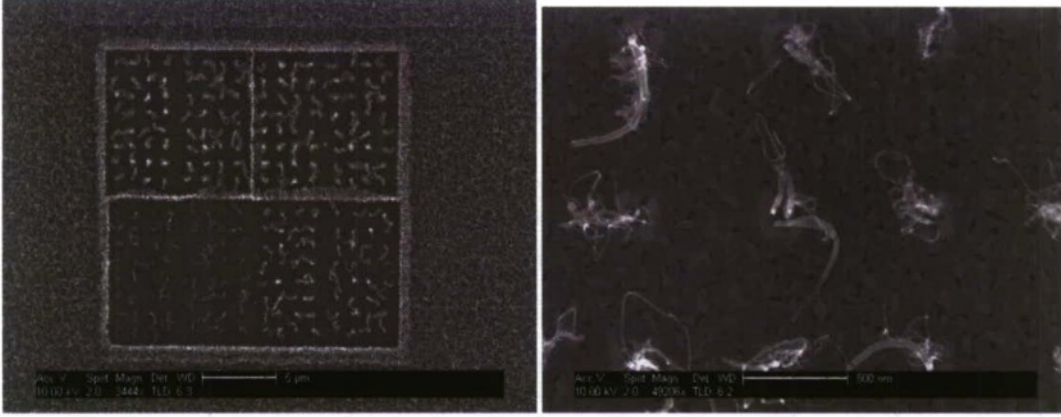


Figure 22: SEM micrographs of nano-scale islands of CNTs at two different magnifications

Quantum Coherence Sensor

The goal of this portion of the study was to analyze the feasibility and physical implementation of quantum coherent optical sensors. As part of the seedling effort, we performed a careful theoretical study on utilizing quantum coherence to perform optical coherence measurement, and identified a physical system and device concept to realize coherence measurement using quantum interactions. The debate on the potential advantage of utilizing quantum systems for direct measurement of optical coherence between two fields with better SNR than the classical limit has not quite been conclusively settled. Based on the technologies available today, physical realization of such coherence measurement remains a major challenge.

Classical interferometry for measuring the mutual coherence function Γ_{12} is illustrated in Fig. 23a. The two optical fields are described by a set of annihilation operators \hat{b}_{k0} and \hat{b}_{k1} with a quasi-monochromatic spectrum featuring a center frequency of ω_c , bandwidth of $\Delta\omega$, and relative phase shift of φ . We assume that the spectrum of the two fields is identical, so that $\Gamma_{11} = \Gamma_{22} = I_0$ and $\langle \hat{b}_{k0}^\dagger \hat{b}_{k1} \rangle = n_k \delta_{kk'}$, where n_k is the mean photon number in the mode k . The normalized mutual coherence $\zeta \equiv \Gamma_{12}/I_0$ characterizes the level of coherence between the modes \hat{b}_{k0} and \hat{b}_{k1} . The irradiance on the detectors are

$$I_{1,2}(\varphi) = I_0 [1 \pm \text{Re}(\zeta e^{i\varphi})].$$

Measurement of $I_{1,2}(\varphi)$ at three distinct values of φ enables independent estimation of the phase and amplitude of Γ_{12} . When $|\zeta|$ is small, the variance of each measurement of $I_{1,2}$ is approximately equal to the variance of measurements of I_0 , given by

$$\sigma_I^2 = 2\eta I_0 (1 + \eta n) \hbar \omega_c / TA,$$

where η is the quantum efficiency of the detector, $n = 1/(e^{\hbar\omega_c/k_B\Theta} - 1)$ is the mean occupation number at ω_c for a source with effective temperature Θ , T is the integration time, and $A = \pi W_0^2$ is the cross-sectional area of the optical fields assumed to be in Gaussian modes with beam waist W_0 . The “noise equivalent coherence” corresponding to $|\Gamma_{12,\min}|^2 = \sigma_I^2$ is a measure of the minimum detectable mutual coherence in the classical system. $|\Gamma_{12,\min}|^2$

is independent of ζ , and the signal-to-noise ratio (SNR) in estimating Γ_{12} degrades as ζ decreases.

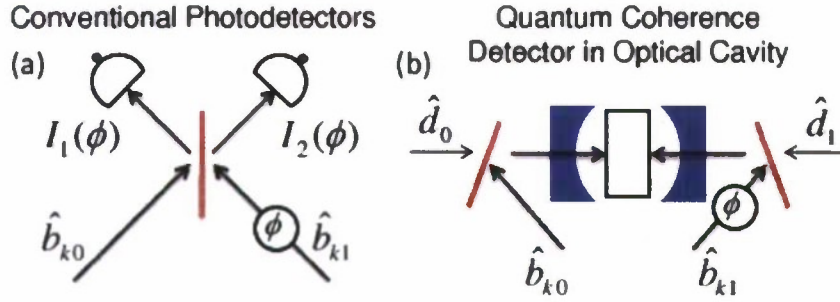


Figure 23: Schematic for sensing mutual coherence using (a) a beam splitter and classical irradiance detectors and (b) quantum coherence detector.

Our model quantum coherence detector replaces the beamsplitter and the two photodetectors (Fig. 23b) with a quantum system directly coupled to the two optical fields. As a physical implementation, we consider a collection of three-level atoms in a small optical cavity whose level structure is shown schematically in Fig. 24a. This system choice provides a pair of stable ground states (e.g., hyperfine levels of an atom with non-zero nuclear spin) that feature long coherence times and negligible inhomogeneous broadening. The excited state (denoted by $|2\rangle$) is coupled to two ground states ($|0\rangle$ and $|1\rangle$) via Raman transition. The transitions between the two ground states and the excited state are chosen to require orthogonal polarization corresponding to the optical fields. We also consider two coherent control beams of frequency ω_1 and ω_2 described by the operators \hat{d}_1 and \hat{d}_2 interacting with the same atoms, where a complete control of the mutual coherence is available by manipulating the intensities and relative phase of the beams. The cavity is necessary to enhance the coupling between the optical fields and the atom, so that the coherent interaction necessary for the coherence of the field to drive the atomic transition occurs within the decoherence time of the atoms due to spontaneous emission.

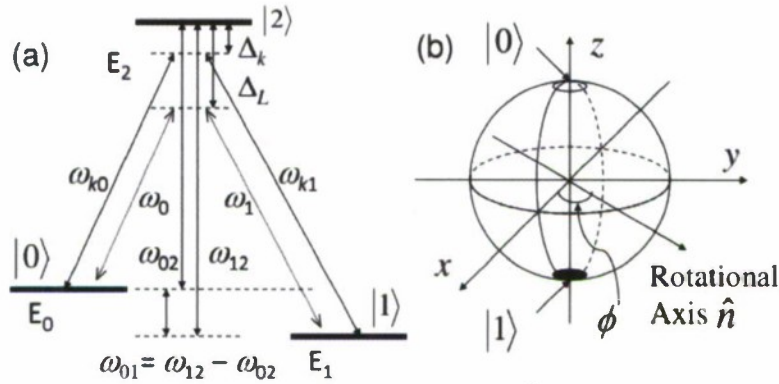


Figure 24: (a) Level structure of the atom under consideration. The two ground states $|0\rangle$ and $|1\rangle$ are coupled via an excited state $|2\rangle$ through optical dipole transitions. (b) Bloch sphere representation of the atomic system. The interaction with the field rotates the initial state around the axis \hat{n} , located on the $x - y$ plane making an angle ϕ with the x -axis, by the angle $2|\Omega_0|T$.

The atomic population dynamics can be modeled using standard Jaynes-Cummings interaction Hamiltonian under adequate approximations. Under the assumption of large detuning ($\Delta_0, \Delta_k \gg \Delta\omega$) and considering time evolution over time scales much longer than the optical bandwidth ($t \gg \Delta\omega$), the probability amplitudes for the two ground states ($C_0(t)$ and $C_1(t)$) satisfy a simple pair of equations

$$\begin{aligned}\dot{C}_0(t) &\simeq i\delta_0 C_0(t) + i\Omega(t)C_1(t), \\ \dot{C}_1(t) &\simeq i\Omega^*(t)C_0(t) + i\delta_1 C_1(t),\end{aligned}$$

where δ_i denotes the AC Stark shifts of each level due to interaction with the optical fields and

$$\Omega(t) \equiv \sum_{k,k'} g_{k,02}^* g_{k',12} \frac{\hat{c}_{k0}^\dagger \hat{c}_{k'1} e^{i[(\omega_{k0} - \omega_{k'1})t + \phi_{k'}]}}{\omega_{k'2} - \omega_{k'1}}$$

is the (complex) Rabi frequency of the system. Under large detuning assumption, the Rabi frequency ensemble-averaged over the bandwidth of the optical fields becomes time-independent and reduces to

$$\Omega_0 \equiv \langle \Omega(t) \rangle \simeq \frac{Z_0 d_{02} d_{12}}{\hbar^2 \Delta} \frac{\omega_{02} \omega_{12}}{\bar{\omega}_0 \bar{\omega}_1} \frac{\mathcal{F}}{\pi} \Gamma_{12}(\tau),$$

where d_{i2} denote the dipole moment between the two atomic states $|i\rangle$ and $|2\rangle$, $\Delta \equiv \langle \Delta_k \rangle$ and $\bar{\omega}_i \equiv \langle \omega_{ki} \rangle$ are the ensemble average values of the detuning and the optical frequency, respectively, taken over the optical field, and the phase difference is taken to be $\phi_k = \omega_{k1} \tau$. Z_0 is the impedance of vacuum, and \mathcal{F} is the finesse of the optical cavity. We further expressed the electric field using the field annihilation operators and used the definition for $\Gamma_{12}(\tau)$. We see that the ensemble-averaged Rabi frequency is proportional to the mutual coherence $\Gamma_{12}(\tau)$ of the two optical fields. If the atoms are prepared in the initial state

$$|\Psi(t=0)\rangle = \cos \alpha |0\rangle + e^{i\beta} \sin \alpha |1\rangle,$$

one can find an exact solution to the equations that describe the atomic population dynamics. When the two levels $|0\rangle$ and $|1\rangle$ are exactly degenerate in the presence of AC Stark shifts ($\delta_0 = \delta_1$), the system undergoes a coherent Rabi oscillation between the two states. If we express the Rabi frequency as $\Lambda_0 \equiv |\Lambda_0| e^{i\varphi}$, the solution simplifies to

$$\begin{aligned}\langle C'_0(t) \rangle &= \cos \alpha \cos |\Omega_0|t + ie^{i(\varphi+\beta)} \sin \alpha \sin |\Omega_0|t, \\ \langle C'_1(t) \rangle &= e^{i\beta} \sin \alpha \cos |\Omega_0|t + ie^{-i\varphi} \cos \alpha \sin |\Omega_0|t.\end{aligned}$$

the dynamics of this two-level atomic system can be described as a qubit on a Bloch sphere, where the two states are represented by the south and north pole, respectively (Fig. 24b). The initial state is a spin coherent state on the Bloch sphere characterized by the polar angle 2ζ and azimuthal angle \mathcal{Q} . The evolution of the atomic state interacting with the optical field over time T corresponds to a rotation around an axis \hat{n} in the $x-y$ plane by the amount $2|\Omega_0|T$. The rotational axis \hat{n} passes through the origin and makes an angle φ with the x -axis.

The solution found above is formally identical to the case when the system is driven

by two coherent states, but with two critical differences. First, the Rabi frequency and AC Stark shifts are given by the ensemble-averaged value over the partially coherent field modes whereas such averaging is not necessary for pure coherent states. Second, the variance of the Rabi frequency is non-zero and the atomic system evolution features fluctuations whereas such fluctuation can be suppressed for the coherent state-driven case. This fluctuation contributes to the SNR of the detection scheme.

Direct measurement of the atomic population after the interaction provides a measure of the observable $|\Gamma_{12}(\tau)|^2$ rather than the mutual coherence $\Gamma_{12}(\tau)$. In order to measure $\Gamma_{12}(\tau)$, we take the approach of adding the two coherent-state control beams to the system to counteract the state evolution caused by the two optical fields under investigation (Fig. 23b). The system evolution is described by including all the terms in the Hamiltonian. The resulting solution is identical in form as above, with the AC Stark shift terms and the Rabi frequency replaced by

$$\delta_i \rightarrow \delta'_i = \delta_i + \delta''_i, \quad \Omega_0 \rightarrow \Omega_T = \Omega_0 + \Omega_1,$$

$$\delta''_i \equiv |g_{i2}|^2 |\alpha_i|^2 / \Delta_L,$$

$$\Omega_1 \equiv g_{02}^* g_{12} \alpha_0^* \alpha_1 e^{-i\psi} / \Delta_L,$$

where α_0 and α_1 are the coherent amplitudes of the two coherent fields and ψ is the phase difference between them. In this approach, the atomic system prepared in a set of well-defined states (e.g., a few states in the equator of the Bloch sphere) interacts with the two unknown fields and the two control fields for a prescribed time T , and then the atomic population is measured in the two basis states $|0\rangle$ and $|1\rangle$ with close to unity quantum efficiency. The amplitudes and relative phase difference between the two coherent control fields are adjusted as the experiment is repeated, until the atomic system evolution is completely suppressed ($\Omega_T = 0$). Under this condition, the coherence of the control fields infers the mutual coherence to be measured ($\Omega_0 = -\Omega_1$).

The sensitivity of this approach to coherence detection is limited by four major noise processes: the fluctuation in the Rabi frequency due to the fluctuation of the optical fields ("photon noise"), the noise associated with determining the coherence of the control beams ("optical readout noise"), the spontaneous emission of the atoms during the Raman process ("spontaneous noise"), and the statistical noise from detection of atomic states, which will be projected to one of the two basis states ("atom shot noise"). The photon noise in atomic evolution is contributed only by the partially coherent fields (and not by coherent control fields), and the variance averaged over the measurement time T is calculated by considering

$$\langle \Omega^2 \rangle = \frac{1}{T^2} \int_0^T dt_1 \int_0^T dt_2 \langle \Omega(t_1) \Omega(t_2) \rangle \simeq \Omega_0^2 \left(1 + \frac{2\pi}{T\Delta\omega} \frac{n+1}{n} \right).$$

The variance in measurement of the mutual coherence due to photon noise is given by $\sigma_p^2 = |\Gamma_{12}|^2 (2\pi/T\Delta\omega)(n+1)/n$. The shot noise corresponding to determining the mutual coherence of the control beams is given by $2I_L(\hbar\omega_L/TA)$, where I_L is the intensity of the laser beam interacting with the atoms. Under the balance condition $I_L/\Delta_L \sim \Gamma_{12}\mathcal{F}/\pi\Delta$, the optical readout noise for the mutual coherence is given by

$$\sigma_L^2 = 2I_L \frac{\hbar\omega_L}{TA} \left(\frac{\Delta}{\Delta_L} \frac{\pi}{\mathcal{F}} \right)^2 \simeq 2|\zeta|n \left(\frac{\hbar\omega_c}{TA} \frac{\pi}{\mathcal{F}} \right)^2 \frac{\Delta\omega T}{2\pi} \frac{\Delta}{\Delta_L},$$

where we assume $\omega_{1,2} \simeq \omega_c \simeq \omega_L$. For the spontaneous noise, we require that the spontaneous emission rate of the upper state of the atom be small compared to the Rabi frequency due to the optical fields, so that the “error” from spontaneous emission during the coherence measurement is small. The corresponding noise is given by

$$\sigma_{sp} \simeq (4\pi^2 \hbar \omega_c \Delta / 3\lambda^2 \mathcal{F}), \text{ where } \lambda = 2\pi/\omega_c \text{ is the central wavelength of the optical fields.}$$

For the atom shot noise, the precision with which one can determine the angle of system rotation is given by the shot noise in the number of atoms detected in each state.

The corresponding variance in mutual coherence is given by $\sigma_a^2 \simeq (\hbar^2 \Delta / d_{02} d_{12} Z_0 T)^2 / N_a$, where d_{i2} is the optical transition dipole moment between the state $|i\rangle$ and $|2\rangle$. The overall variance of mutual coherence detection in the quantum coherence detector is given by $\sigma_Q^2 = \sigma_p^2 + \sigma_L^2 + \sigma_{sp}^2 + \sigma_a^2$.

In the Gaussian beam geometry with a beam waist of W_0 , the sensitivity enhancement factor $Q_{mc} \equiv \sigma_I^2 / \sigma_Q^2$ defined as the improvement over classical interferometric approaches

$$Q_{mc} \simeq \left[\frac{|\zeta|^2}{2} + \left(\frac{\pi}{\mathcal{F}} \right)^2 \left\{ \frac{|\zeta|\Delta}{2(n+1)\Delta_L} + \frac{32\pi^4 \Delta^2 A^2 n_T}{9\lambda^4 n^2 (n+1) \Delta \omega^2} + \left(\frac{\hbar}{Z_0 d_{02} d_{12} \omega_c} \right)^2 \frac{\lambda}{4N_0(1+n)n_T} \right\} \right]^{-1}.$$

where $n_T = n\Delta\omega T/2\pi$ is the total number of photons detected per measurement time interval T , and an efficient irradiance detector was assumed ($\eta = 1$). Figure 25 shows Q_{mc} as a function of n_T assuming small volume cavity with high finesse, using typical values of $d_{02} = d_{12} \simeq 1.6 \times 10^{-29} \text{ Cm}$, $\Delta\omega \sim 10^{-7} \omega_c$, $\lambda = 780 \text{ nm}$, $N_0 \sim 10^{18} \text{ m}^{-3}$ is the density of the atoms, $W_0 = 1 \text{ } \mu\text{m}$, and $\mathcal{F} = 1.6 \times 10^5$.

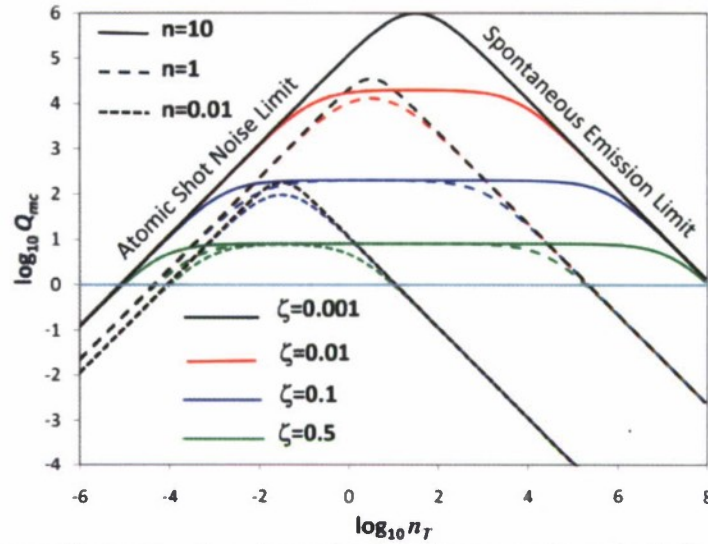


Figure 25: Enhancement factor Q_{mc} of quantum coherence sensor over classical interference detectors plotted as a function of n_T . Solid, dashed and dotted lines represent the average number of photons per mode $n = 10, 1$ and 0.01 , respectively, while the green, blue, red and black curves correspond to ζ values of $1, 0.1, 0.01$ and 0.001 , respectively.

At low n_T , the sensitivity of the quantum coherence detector is limited by the atom shot noise, and is below that of classical interferometric detector. As the average photon number per mode n increases, the thermal noise in the optical fields increases and the quantum coherence detector performance improves as the SNR in classical measurement degrades (dotted, dashed and solid curves). The noise performance of the quantum detector improves as n_T increases, until it is limited by the optical readout noise or the photonic noise limit. In this limit, the dependence of noise on n_T is identical for the quantum and classical case, so the enhancement factor Q_{mc} remains constant as a function of n_T . In classical interferometry, the noise is determined by the photon noise corresponding to the irradiance of each optical field (Γ_{11} and Γ_{22}), while in the quantum case the noise contribution only comes from the amount of mutual coherence present between the two fields. When the mutual coherence is very small between two fields with low average photon number per mode, the quantum coherence detector sensitivity is higher by a factor of $1/\zeta^2$. At higher values of n_T , longer integration time increases the probability of spontaneous emission and the sensitivity is determined by the spontaneous emission noise.

Through our theoretical analysis, we have effectively proposed a “coherence interferometer” where the mutual coherence between two optical fields interferes with the mutual coherence of two control fields (prepared in coherent states). The mutual coherence of the control fields can be manipulated at will, and we balance the coherence interferometer so that the mutual coherences of the pairs of fields destructively interfere. This provides a means to quantitatively estimate the mutual coherence in the signal fields. There has been some debate on whether the noise in the signal fields impacts the variances of coherent rotations of the atomic system that accommodates the interference. Our analysis shows that the impact of the intensity noise from individual fields does not impact the coherent rotations, but it was pointed out that the variance in the rotation angle of the atomic system should be evaluated by considering a fourth-order coherence func-

tion of the Rabi rotation angle Ω (which will be an 8-th order coherence function of the optical fields). Whether such higher order coherence functions impact the performance of coherence interferometer has not been analyzed at this point.

The experimental condition that has to be satisfied to realize such coherence interferometer seems to be extremely challenging, mostly because the coherent interaction between the natural fields (the signal fields) and the (far-detuned) atomic resonance is necessarily very weak. Spontaneous emission will lead to decoherence of the coherence interferometer unless the interaction can be dramatically enhanced. The use of high finesse optical cavity could address this issue, but will lead to constraint on the bandwidth of the signal fields. One has to distinguish the effect of severe filtering from the cavity (that enhances coherence) and the improved sensitivity of our coherence detector due to enhanced interaction by the cavity. Our assumptions operate in the regime where the cavity bandwidth is still large compared to the bandwidth of the signal fields and demonstrate the benefits of the mutual coherence interferometer. The remaining conditions of the experiments, including the atomic density and coherence times required, makes this an extremely challenging experiment to perform in reality.

Compressive Holography

Compressive measurement was the second emphasis of the coherence measurement portion of this program. We realized in early 2009 that compressive inference strategies developed in support of CASSI imaging could be applied to form tomographic images from single frame Gabor holograms. We demonstrated this capacity in stand-off lensless imaging in [3]. As a second demonstration, we demonstrated 3D reconstruction of a microscopic object from a single 2D Gabor hologram produced by the microscope with a point source. For compactness, these microscopes typically use the Gabor geometry rather than the Leith-Upatneik's geometry. This causes the undesirable autocorrelation and twin-image problems. Hence, our goals are two-fold: 1) to solve the underdetermined problem of obtaining a 3D tomographic reconstruction from a 2D hologram, and 2) to remove the autocorrelation and twin-image problems that often severely deteriorate the visual quality of the reconstruction.

Figure 26 shows the system schematic of compressive holographic microscope. A coherent light is spatially filtered and collimated to make a plane wave and this plane wave is focused to make a point source by a microscope. From this point source, a sample is illuminated and magnified at the FPA. The recorded interferogram on FPA is the Gabor hologram with the spherical wave.

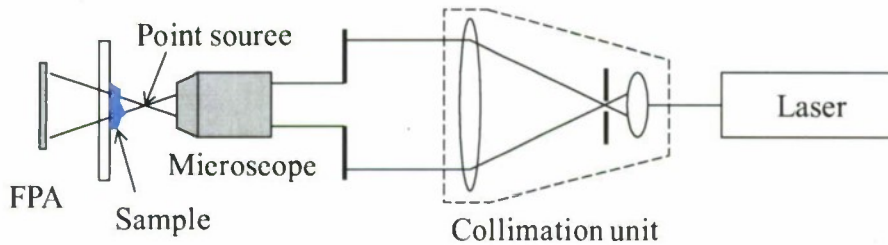


Fig. 26. Schematic of compressive holographic lensless microscope

In the Gabor geometry, the intensity measurement on FPA is expressed as

$$I(x, y; z) = |A(x, y; z) + E(x, y; z)|^2 \quad (1)$$

$$= |A(x, y; z)|^2 + |E(x, y; z)|^2 + A^*(x, y; z)E(x, y; z) + A(x, y; z)E^*(x, y; z),$$

where A is the reference field with spherical phase profile from the point source at $z = z_0$ and E is the scattered object field. This scattered field from a 3D object density β can be defined by the first Born approximation as

$$E(x, y; z) = \iiint dx' dy' dz' \beta(x', y', z') A(x', y', z') h(x - x', y - y', z - z'). \quad (2)$$

Here, h is a propagation kernel and Fourier transform of this propagation kernel is given by

$$H(k_x, k_y; z - z') = \exp\left[j(z - z')\sqrt{k^2 - k_x^2 - k_y^2}\right]. \quad (3)$$

The detector plane is positioned at $z=0$. Since this propagation is linear operation, the Gabor hologram can be represented as

$$g = 2 \operatorname{Re}\{Hf\} + e + n, \quad (4)$$

where f is the discrete form of β . e denotes the autocorrelation of A and E , and n is additive noise. In Eq. (4), by enforcing a sparsity constraint on the total variation, the discrete object density f is estimated as

$$\hat{f} = \arg \min_f (\|g - Hf\|^2 + \|f\|_{TV}). \quad (5)$$

Here, $\|f\|_{TV}$ is total variation norm of vector f and defined as

$$\|f\|_{TV} = \sum_z \sum_x \sum_y |(\nabla f_z)_{x,y}|, \quad (6)$$

where f_z denotes a 2D plane of the 3D object datacube.

We demonstrated compressive holographic microscopy using a He-Ne laser with 632.8nm wavelength as a light source. A microscope with 0.65NA is applied. The focal plane array is a Lumenera CMOS sensor with 1280×1040 resolution, 5.2 μm pixel pitch and 10 bit digitization. Figure 27 shows the experimental setup and a structure of the lensless microscopy. The positions of the microscope and the sample are adjustable with 3-axis stages.

In this system, the magnification is determined by the ratio of effective distances from the point source to the sample and from the point source to the FPA. The numerical aperture (NA) of this system is a function of pixel pitch of FPA, the wavelength, and the magnification. As the most simple magnification system, the NA of 4f optics is given as

$$NA_{4f} = \left(1 + \frac{4p^2 - \lambda^2}{M^2 \lambda^2}\right)^{-0.5}, \quad (7)$$

where M is magnification, and p is the pixel pitch of FPA. The NA of this system is larger than that in a magnification system with 4f optics even though the wave recorded on FPA has a spherical phase. The optical magnification is set as 4.5 and then the NA is 0.27, which yields axial resolution $\Delta_z = 2\lambda/NA^2 = 16.9\mu\text{m}$ and transverse resolution

$$\Delta_x = \lambda/2NA = 1.15\mu\text{m}.$$

As a sample, a water flea with a 1.5mm size is measured using a snap shot. Figure 28 shows a raw Gabor hologram and reconstruction images. The transverse slices at various ranges with back propagated fields and compressive holography are shown respectively

in Figs. 28(b) and (c), where each interval between adjacent slices is 0.3mm . In the slices with compressive holography, the antenna structures are clearly shown with the efficient removal of the autocorrelation and twin-image terms in comparison of the images with back propagated fields.

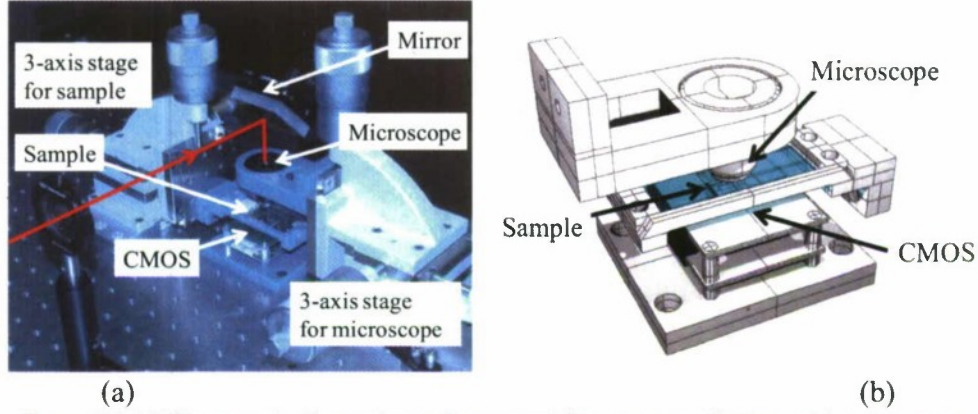


Figure 27. (a) Photograph of experimental setup and (b) structure of holographic microscopy.

We demonstrated the feasibility in obtaining a 3D reconstruction of a microscopic object from a single 2D Gabor hologram produced by a holographic microscope. In Figs. 28(b) and (c), the reconstruction images with back propagated fields shows severely deteriorated images, but the images with compressive holography shows the clear antenna structure, since the linear twin image term and splits the non-linear autocorrelation term in the measurement plane are significantly removed. However, there are only small differences among slices of datacube even though the distance between slices are enough longer than axial resolution. We conjecture that the reason is that the object is rather thick in comparing the transverse resolution and the radiation scattered from object has narrow distribution. The edge in the body of the specimen is only observable in reconstruction images, since the Gabor hologram is hard to measure the part of object with uniformly low transmission in large area. The reconstruction errors and the effects of noise usually results from the insufficient number of measurements. It would be desirable to combine this system with synthetic aperture technique or structured illumination for increasing the number of measurements.

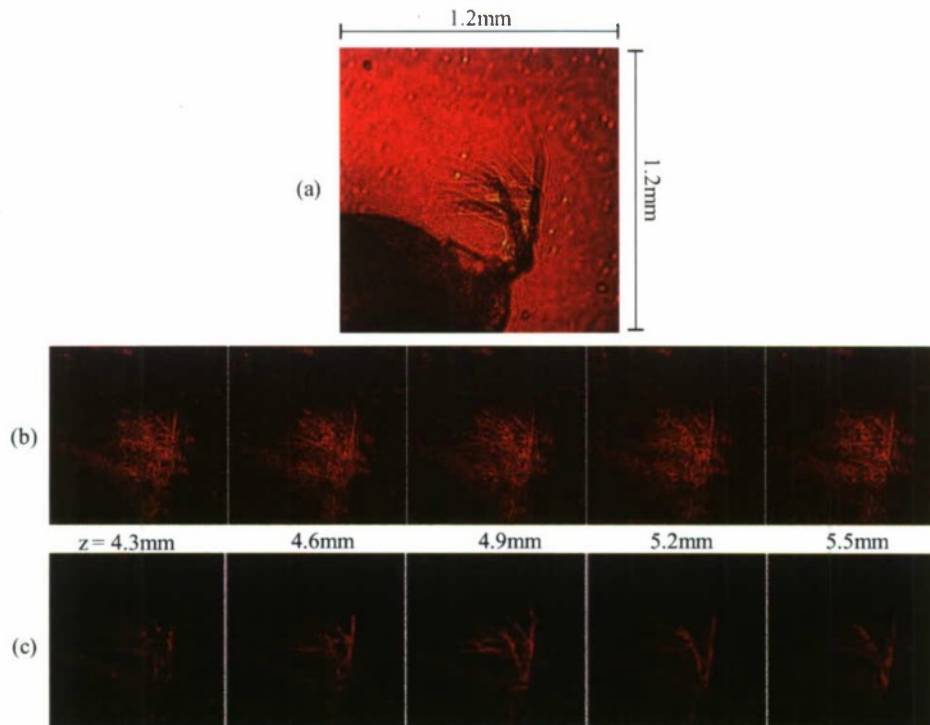


Fig. 28. (a) Raw Gabor hologram measuring a water flea, (b) transverse slices at various ranges with back propagated fields, and (c) transverse slices at various ranges with compressive holography.

5. Personnel Supported:

D.J. Brady
 Nan Zheng
 C. Fernandez
 Ashwin Wagadarikar
 Jeffrey T. Glass
 Scott Wolter
 Billyde Brown
 Jungsang Kim
 Se Hoon Lim
 Kerkil Choi

6. Publications:

1. C.Fernandez, B.D. Guenther, M.E. Gehm, M.E. Sullivan, and D.J. Brady, "Longwave Infrared (LWIR) Coded Aperture Dispersive Spectrometer", *Optics Express*, Vol. **15**, Issue 9, pp. 5742-5753 (April 2007).

2. M. E. Gehm, M. S. Kim, C. Fernandez, and D. J. Brady, "High-throughput, multiplexed pushbroom hyperspectral microscopy," *Opt. Express* **16**, 11032-11043 (2008)
3. Gehm, M.E. and Brady, D.J., *High-throughput hyperspectral microscopy*, Proceedings of SPIE - The International Society for Optical Engineering, vol. 6090 (2006), pp. 609007-, San Jose, CA, United States [[12.644828](#)]
4. M.E. Gehm, R. John, D.J. Brady, R.M. Willet, and T.J. Schulz,, "Single-shot compressive spectral imaging with a dual-disperser architecture," *Opt. Express* **15**, 14013-14027 (2007)
5. Fernandez, C.A., et al., Fluorescence microscopy with a coded aperture snapshot spectral imager. *Proc SPIE*, 2009. **7184-33**: p. 1-11
6. Christy Fernandez Cull, Kerkil Choi, David J. Brady, and Tim Oliver, "Identification of fluorescent beads using a coded aperture snapshot spectral imager," *Appl. Opt.* **49**, B59-B70 (2010)
7. Cull, C.F., et al., *Direct fluorescence spectral feature identification using a coded aperture snapshot spectral imager*. *Optics Express*, 2009.
8. Brown, B., et al., *Growth of aligned bamboo-structured carbon nanotubes via platinum catalyst*, in preparation for Nanoletters.

7. Interactions/Transitions:

a. Participation/presentations at meetings, conferences, seminars, etc.

K. Choi, R. Horisaki, D. Marks, and D. Brady, "Coding and Signal Inference in Compressive Holography," in *Computational Optical Sensing and Imaging*, OSA Technical Digest (CD) (Optical Society of America, 2009), paper CThA5.

S. Lim, R. Horisaki, K. Choi, D. Marks, and D. Brady, "Experimental Demonstrations of Compressive Holography," in *Computational Optical Sensing and Imaging*, OSA Technical Digest (CD) (Optical Society of America, 2009), paper CThA6.

A. Wagadarikar, D. Marks, K. Choi, and D. Brady, "Compressive Coherence Sensing," in *Computational Optical Sensing and Imaging*, OSA Technical Digest (CD) (Optical Society of America, 2009), paper CTuA6.

C. A. Fernandez, S. Lim, B. D. Guenther, D. J. Brady, and S. T. McCain, "High-Throughput, Multiplex Aperture-Coded Raman Spectrometer for Biomedical Diagnostics," in *Biomedical Optics*, OSA Technical Digest (CD) (Optical Society of America, 2008), paper BTuF15.

Materials Research Society, Materials Research 2008, North Carolina, Organizing Committee, November 18. 2008

Bouchet Society (for underrepresented minority graduate students in the natural sciences engineering, and mathematics), Duke University, Poster Presentation, Billyde Brown et al.

Materials Research Society, Materials Research 2008, North Carolina, Organizing Committee, November 18. 2008, Poster Presentation, Billyde Brown et al.

b. Consultative and advisory functions

Panelist, STaR (Science, Technology and Research) Symposium, April 14-15, Charleston, West Virginia

c. Technology Assists, Transitions, and Transfers.

Coded aperture snapshot spectral imaging systems derived from research under this program have been developed in prototype form for several users by Applied Quantum Technologies, Inc. A competitive test of this technology with conventional spectral imagers is scheduled with the National Geospatial Agency for June 2010. A CASSI system is also scheduled for delivery at the Peabody Museum at Yale University in 2010. CASSI has proven to be a unique and useful approach for rapid spectral image capture, we anticipate continuing transitions. Compressive holography studies under this program led to a new DARPA MTO seedling program in holographic remote sensing (collaboration with the University of Rochester.) Compressive holography results were also presented at the industry day for DARPA's Fine Domain Optical Surveillance (FDOS) program. Compressive holography is a component of system design for several FDOS projects.

8. New discoveries, inventions, or patent disclosures.

CNT growth using Pt catalyst has crossover application in the area of nerve stimulation. Thus, an Invention Disclosure has been submitted entitled: *"Biocompatible Nanostructured Coating To Reduce Risks Of Physiological Harm And Material Damage Of Implantable Electrodes During Chronic Nerve Stimulation Therapy"*

9. Honors/Awards:

Nan Zheng passed PhD preliminary exam 4/21/08

C. Fernández (National Defense and Engineering Graduate Fellowship)

A. Wagadarikar (Natural Sciences and Engineering Research Council [NSERC] of Canada Fellowship)

References

1. Fernandez, C.A., et al., *Fluorescence microscopy with a coded aperture snapshot spectral imager*. Proc SPIE, 2009. **7184-33**: p. 1-11. Christy Fernandez Cull, Kerkil Choi, David J. Brady, and Tim Oliver, "Identification of fluorescent beads using a coded aperture snapshot spectral imager," Appl. Opt. 49, B59-B70 (2010)
2. Cull, C.F., et al., *Direct fluorescence spectral feature identification using a coded aperture snapshot spectral imager*. Optics Express, 2009.
3. David J. Brady, Kerkil Choi, Daniel L. Marks, Ryoichi Horisaki, and Sehoon Lim, "Compressive Holography," Opt. Express 17, 13040-13049 (2009).